

# Improving optical contact for functional near-infrared brain spectroscopy and imaging with brush optodes

Bilal Khan,<sup>1,\*</sup> Chester Wildey,<sup>2</sup> Robert Francis,<sup>3</sup> Fenghua Tian,<sup>1</sup> Mauricio R. Delgado,<sup>4,5</sup> Hanli Liu,<sup>1</sup> Duncan MacFarlane,<sup>3</sup> and George Alexandrakis<sup>1</sup>

<sup>1</sup>Department of Bioengineering, University of Texas at Arlington, 500 UTA Boulevard, Arlington, Texas 76010, USA

<sup>2</sup>MRRA Inc., 3621 Smoke Tree Trail, Euless, Texas 76040, USA

<sup>3</sup>Department of Electrical Engineering, University of Texas at Dallas, 800 West Campbell Road, Richardson, Texas 75080, USA

<sup>4</sup>Department of Neurology, Texas Scottish Rite Hospital for Children, 2222 Welborn Street, Dallas, Texas 75219, USA

<sup>5</sup>Department of Neurology, University of Texas Southwestern Medical Center at Dallas, 5901 Forest Park Road, Dallas, Texas 75390, USA

\*bilal.khan@mavs.uta.edu

**Abstract:** A novel brush optode was designed and demonstrated to overcome poor optical contact with the scalp that can occur during functional near infrared spectroscopy (fNIRS) and imaging due to light obstruction by hair. The brush optodes were implemented as an attachment to existing commercial flat-faced (conventional) fiber bundle optodes. The goal was that the brush optodes would thread through hair and improve optical contact on subjects with dense hair. Simulations and experiments were performed to assess the magnitude of these improvements. FNIRS measurements on 17 subjects with varying hair colors (blonde, brown, and black) and hair densities (0–2.96 hairs/mm<sup>2</sup>) were performed during a finger tapping protocol for both flat and brush optodes. In addition to reaching a study success rate of almost 100% when using the brush optode extensions, the measurement setup times were reduced by a factor of three. Furthermore, the brush optodes enabled improvements in the activation signal-to-noise ratio (SNR) by up to a factor of ten as well as significant ( $p < 0.05$ ) increases in the detected area of activation (dAoA). The measured improvements in SNR were matched by Monte Carlo (MC) simulations of photon propagation through scalp and hair. In addition, an analytical model was derived to mathematically estimate the observed light power losses due to different hair colors and hair densities. Interestingly, the derived analytical formula produced excellent estimates of the experimental data and MC simulation results despite several simplifying assumptions. The analytical model enables researchers to readily estimate the light power losses due to obstruction by hair for both flat-faced fiber bundles and individual fibers for a given subject.

© 2012 Optical Society of America

**OCIS codes:** (170.2655) Functional monitoring and imaging; (170.3880) Medical and biological imaging; (300.6340) Spectroscopy, infrared.

## References and links

1. X. Bai, Z. Liu, N. Zhang, W. Chen, and B. He, "Three-dimensional source imaging from simultaneously recorded ERP and BOLD-fMRI," *IEEE Trans. Neural Syst. Rehabil. Eng.* **17**(2), 101–106 (2009).
2. K. Li, L. Guo, J. Nie, G. Li, and T. Liu, "Review of methods for functional brain connectivity detection using fMRI," *Comput. Med. Imaging Graph.* **33**(2), 131–139 (2009).
3. G. Muehllehner and J. S. Karp, "Positron emission tomography," *Phys. Med. Biol.* **51**(13), R117–R137 (2006).
4. B. Dilharreguy, R. A. Jones, and C. T. Moonen, "Influence of fMRI data sampling on the temporal characterization of the hemodynamic response," *Neuroimage* **19**(4), 1820–1828 (2003).

5. T. J. Huppert, R. D. Hoge, S. G. Diamond, M. A. Franceschini, and D. A. Boas, "A temporal comparison of BOLD, ASL, and NIRS hemodynamic responses to motor stimuli in adult humans," *Neuroimage* **29**(2), 368–382 (2006).
6. F. Abdelnour, B. Schmidt, and T. J. Huppert, "Topographic localization of brain activation in diffuse optical imaging using spherical wavelets," *Phys. Med. Biol.* **54**(20), 6383–6413 (2009).
7. S. P. Koch, C. Habermehl, J. Mehnert, C. H. Schmitz, S. Holtze, A. Villringer, J. Steinbrink, and H. Obrig, "High-resolution optical functional mapping of the human somatosensory cortex," *Front Neuroenergetics* **2**, 12 (2010).
8. M. Izzetoglu, A. Devaraj, S. Bunce, and B. Onaral, "Motion artifact cancellation in NIR spectroscopy using Wiener filtering," *IEEE Trans. Biomed. Eng.* **52**(5), 934–938 (2005).
9. C. Terborg, K. Gröschel, A. Petrovitch, T. Ringer, S. Schnaudigel, O. W. Witte, and A. Kastrup, "Noninvasive assessment of cerebral perfusion and oxygenation in acute ischemic stroke by near-infrared spectroscopy," *Eur. Neurol.* **62**(6), 338–343 (2009).
10. T. Suto, M. Fukuda, M. Ito, T. Uehara, and M. Mikuni, "Multichannel near-infrared spectroscopy in depression and schizophrenia: cognitive brain activation study," *Biol. Psychiatry* **55**(5), 501–511 (2004).
11. B. Khan, F. Tian, K. Behbehani, M. I. Romero, M. R. Delgado, N. J. Clegg, L. Smith, D. Reid, H. Liu, and G. Alexandrakakis, "Identification of abnormal motor cortex activation patterns in children with cerebral palsy by functional near-infrared spectroscopy," *J. Biomed. Opt.* **15**(3), 036008 (2010).
12. F. Tian, M. R. Delgado, S. C. Dhamne, B. Khan, G. Alexandrakakis, M. I. Romero, L. Smith, D. Reid, N. J. Clegg, and H. Liu, "Quantification of functional near infrared spectroscopy to assess cortical reorganization in children with cerebral palsy," *Opt. Express* **18**(25), 25973–25986 (2010).
13. D. H. Burns, S. Rosendahl, D. Bandilla, O. C. Maes, H. M. Chertkow, and H. M. Schipper, "Near-infrared spectroscopy of blood plasma for diagnosis of sporadic Alzheimer's disease," *J. Alzheimers Dis.* **17**(2), 391–397 (2009).
14. A. Gibson and H. Dehghani, "Diffuse optical imaging," *Philos. Transact. A Math. Phys. Eng. Sci.* **367**(1900), 3055–3072 (2009).
15. M. Kubota, M. Inouchi, I. Dan, D. Tsuzuki, A. Ishikawa, and T. Scovel, "Fast (100–175 ms) components elicited bilaterally by language production as measured by three-wavelength optical imaging," *Brain Res.* **1226**, 124–133 (2008).
16. Q. Zhang, X. Yan, and G. E. Strangman, "Development of motion resistant instrumentation for ambulatory near-infrared spectroscopy," *J. Biomed. Opt.* **16**(8), 087008 (2011).
17. H. W. Schydtz, K. Ciftçi, A. Akin, M. Ashina, and H. Bolay, "Intact neurovascular coupling during executive function in migraine without aura: interictal near-infrared spectroscopy study," *Cephalalgia* **30**(4), 457–466 (2010).
18. F. Orihuela-Espina, D. R. Leff, D. R. James, A. W. Darzi, and G. Z. Yang, "Quality control and assurance in functional near infrared spectroscopy (fNIRS) experimentation," *Phys. Med. Biol.* **55**(13), 3701–3724 (2010).
19. A. V. Medvedev, J. M. Kainerstorfer, S. V. Borisov, A. H. Gandjbakhche, and J. Vanmeter, "Seeing" electroencephalogram through the skull: imaging prefrontal cortex with fast optical signal," *J. Biomed. Opt.* **15**(6), 061702 (2010).
20. T. Funane, M. Kiguchi, H. Atsumori, H. Sato, K. Kubota, and H. Koizumi, "Synchronous activity of two people's prefrontal cortices during a cooperative task measured by simultaneous near-infrared spectroscopy," *J. Biomed. Opt.* **16**(7), 077011 (2011).
21. S. M. Liao, N. M. Gregg, B. R. White, B. W. Zeff, K. A. Bjerkaas, T. E. Inder, and J. P. Culver, "Neonatal hemodynamic response to visual cortex activity: high-density near-infrared spectroscopy study," *J. Biomed. Opt.* **15**(2), 026010 (2010).
22. B. Khan, C. Wildey, R. Francis, F. Tian, M. I. Romero, M. R. Delgado, N. J. Clegg, L. Smith, H. Liu, D. L. MacFarlane, and G. Alexandrakakis, "Functional near infrared brain imaging with a brush-fiber optode to improve optical contact on subjects with dense hair," *Proc. SPIE* **7883**, 78834V (2011).
23. J. M. Barman, I. Astore, and V. Pecoraro, "The normal trichogram of the adult," *J. Invest. Dermatol.* **44**, 233–236 (1965).
24. M. A. Franceschini, D. K. Joseph, T. J. Huppert, S. G. Diamond, and D. A. Boas, "Diffuse optical imaging of the whole head," *J. Biomed. Opt.* **11**(5), 054007 (2006).
25. C. Julien, "The enigma of Mayer waves: Facts and models," *Cardiovasc. Res.* **70**(1), 12–21 (2006).
26. J. Selb, J. J. Stott, M. A. Franceschini, A. G. Sorensen, and D. A. Boas, "Improved sensitivity to cerebral hemodynamics during brain activation with a time-gated optical system: analytical model and experimental validation," *J. Biomed. Opt.* **10**(1), 011013 (2005).
27. N. M. Gregg, B. R. White, B. W. Zeff, A. J. Berger, and J. P. Culver, "Brain specificity of diffuse optical imaging: improvements from superficial signal regression and tomography," *Front Neuroenergetics* **2**, 0000–9999 (2010).
28. G. Morren, U. Wolf, P. Lemmerling, M. Wolf, J. H. Choi, E. Gratton, L. De Lathauwer, and S. Van Huffel, "Detection of fast neuronal signals in the motor cortex from functional near infrared spectroscopy measurements using independent component analysis," *Med. Biol. Eng. Comput.* **42**(1), 92–99 (2004).
29. Q. Zhang, E. N. Brown, and G. E. Strangman, "Adaptive filtering for global interference cancellation and real-time recovery of evoked brain activity: a Monte Carlo simulation study," *J. Biomed. Opt.* **12**(4), 044014 (2007).
30. B. Khan, P. Chand, and G. Alexandrakakis, "Spatiotemporal relations of primary sensorimotor and secondary motor activation patterns mapped by NIR imaging," *Biomed. Opt. Express* **2**(12), 3367–3386 (2011).
31. T. J. Huppert, S. G. Diamond, M. A. Franceschini, and D. A. Boas, "HomER: a review of time-series analysis methods for near-infrared spectroscopy of the brain," *Appl. Opt.* **48**(10), D280–D298 (2009).

32. B. Brooksby, S. Srinivasan, S. Jiang, H. Dehghani, B. W. Pogue, K. D. Paulsen, J. Weaver, C. Kogel, and S. P. Poplack, "Spectral priors improve near-infrared diffuse tomography more than spatial priors," *Opt. Lett.* **30**(15), 1968–1970 (2005).
33. A. Li, Q. Zhang, J. P. Culver, E. L. Miller, and D. A. Boas, "Reconstructing chromosphere concentration images directly by continuous-wave diffuse optical tomography," *Opt. Lett.* **29**(3), 256–258 (2004).
34. C. F. Beckmann, M. Jenkinson, and S. M. Smith, "General multilevel linear modeling for group analysis in fMRI," *Neuroimage* **20**(2), 1052–1063 (2003).
35. A. F. Abdelnour and T. Huppert, "Real-time imaging of human brain function by near-infrared spectroscopy using an adaptive general linear model," *Neuroimage* **46**(1), 133–143 (2009).
36. A. K. Singh and I. Dan, "Exploring the false discovery rate in multichannel NIRS," *Neuroimage* **33**(2), 542–549 (2006).
37. S. H. Tseng, P. Bargo, A. Durkin, and N. Kollias, "Chromophore concentrations, absorption and scattering properties of human skin in-vivo," *Opt. Express* **17**(17), 14599–14617 (2009).
38. F. Jimenez, A. Izeta, and E. Poblet, "Morphometric analysis of the human scalp hair follicle: practical implications for the hair transplant surgeon and hair regeneration studies," *Dermatol. Surg.* **37**(1), 58–64 (2011).
39. A. Kharin, B. Varghese, R. Verhagen, and N. Uzunbajakava, "Optical properties of the medulla and the cortex of human scalp hair," *J. Biomed. Opt.* **14**(2), 024035 (2009).
40. D. J. Cuccia, F. Bevilacqua, A. J. Durkin, F. R. Ayers, and B. J. Tromberg, "Quantitation and mapping of tissue optical properties using modulated imaging," *J. Biomed. Opt.* **14**(2), 024012 (2009).
41. R. C. Haskell, L. O. Svaasand, T. T. Tsay, T. C. Feng, M. S. McAdams, and B. J. Tromberg, "Boundary conditions for the diffusion equation in radiative transfer," *J. Opt. Soc. Am. A* **11**(10), 2727–2741 (1994).
42. F. K. Knoll, *Radiation Detection and Measurement* (Wiley, New York, 1988).
43. W. F. Cheong, S. A. Prahl, and A. J. Welch, "A review of the optical properties of biological tissues," *IEEE J. Quantum Electron.* **26**(12), 2166–2185 (1990).
44. D. Yudovsky and L. Pilon, "Modeling the local excitation fluence rate and fluorescence emission in absorbing and strongly scattering multilayered media," *Appl. Opt.* **49**(31), 6072–6084 (2010).

## 1. Introduction

Non-invasive sensing and imaging technologies applied to the investigation of brain function in health and disease are of great utility to both clinicians and basic scientists alike. In current clinical settings, the most widely disseminated technologies are electroencephalography (EEG), functional magnetic resonance imaging (fMRI) and positron emission tomography (PET) [1–3]. Each of these technologies comes with its own strengths and limitations. EEG detects the electrical activity from evoked potentials of cortical neurons at high temporal resolution (milliseconds) but cannot detect electrical signals from deep within the brain [1]. Both PET and fMRI can image the entire head volume and provide information about brain function, but with a temporal resolution of 0.5 seconds or longer [3,4]. In addition, all these modalities require relative immobilization of the subject and are sensitive to motion artifacts. Recently functional near infrared spectroscopy (fNIRS) has been found to be a useful alternative technology for studying brain function in healthy subjects [5–8] and ones affected by a wide range of different pathologies such as stroke, depression, cerebral palsy, and Alzheimer's [9–13]. Though this optical technology is limited to cortical imaging at a modest spatial resolution of about 1 cm [14], it can potentially offer high activation-related signal detection sensitivity at high temporal resolution, in the hundreds of milliseconds [15], and a relative robustness to motion artifacts [16].

fNIRS detects the changes in light absorption and scattering in tissue caused by changes in concentration of oxyhemoglobin ( $\Delta\text{HbO}$ ) and deoxyhemoglobin ( $\Delta\text{Hb}$ ) secondary to neuronal activity, through a neurovascular coupling mechanism that is currently under investigation [17]. Though fNIRS can measure the slow hemodynamic response elicited by neuronal activity that correlates with corresponding fMRI measurements [5], it is often the case that the activation signal-to-noise ratio (SNR) in fNIRS is low due to poor optical contact between the optical fibers that deliver and collect near infrared (NIR) light to and from the scalp [18].

The main suspected contributor to poor optical contact is the subjects' hair, especially for dark hair colors and high hair root densities [18], though to our knowledge, no systematic studies have been performed to date to assess quantitatively the effect of these factors on the fNIRS SNR. In addition, during setup of the optical fibers onto a person's head, the hair needs to be parted in order for the optodes to have good optical contact with the scalp, which is time consuming and becomes more difficult for higher spatial resolution studies requiring denser

probe geometries. Due to these limitations, many studies have been restricted to the prefrontal cortex or to measurements on subjects with low hair density [19–21].

In this work, we present a novel brush-fiber optode that was used as an attachment to the light collection end of the detector fiber bundles of a commercial fNIRS continuous wave (CW) imaging system to help overcome poor optical contact while also improving measurement setup times. The brush optode consisted of a bundle of optical fibers that were kept loose, like a hair brush, so that individual optical fibers could easily thread through a subject's hair and reach the scalp. In comparison to our previous work [22], in which the brush-fiber optode was tested on a tissue-simulating phantom and a single subject, measurements in this study were performed with the brush-fiber attachment in place, and without it, on subjects with a wide range of hair colors and hair root densities. Comparisons in measurement setup times, the activation SNR of detected fNIRS time-series signals and the contrast to background ratio (CBR) and detected area of activation (dAoA) of reconstructed images were performed between measurements with and without the brush fiber attachments for each subject. Monte Carlo (MC) simulations were also performed for different hair colors and densities, for both brush and traditional solid fiber bundle optodes, to model the attenuation that NIR light experiences as it travels through layers of hair and hair roots embedded within a few millimeters (mm) into the scalp. Lastly, an analytical formula was derived to mathematically estimate light power losses due to hair obstruction. This formula takes into account the successive attenuation losses that NIR light experiences as it exits the scalp, travels through hair layers, and enters the light collecting optodes. This work presents, to our knowledge, the first attempt to quantify the effect of hair on NIR light signal attenuation and proposes a novel tool to help resolve this common problem in the fNIRS field.

## 2. Methods and materials

### 2.1. Experimental measurements

#### 2.1.1. Subjects

Seventeen subjects [4 long hair (female) and 13 short hair (male);  $25.06 \pm 6.16$  years old] were included in this study. Among these subjects, two were bald, four had blonde hair, four had brown hair, and seven had black hair. Both bald subjects originally had black hair. The subjects' hair densities were in the 0–2.96 hairs/mm<sup>2</sup> range, which spanned the known hair density range found in a previous large population study [23]. For analysis purposes, the hair densities were binned into 0 hairs/mm<sup>2</sup> (bald subjects), 1.8 hairs/mm<sup>2</sup> (1.7–1.9 hairs/mm<sup>2</sup>), 2.2 hairs/mm<sup>2</sup> (2.1–2.3 hairs/mm<sup>2</sup>), and 2.8 hairs/mm<sup>2</sup> (2.7–2.96 hairs/mm<sup>2</sup>) categories. Among these subjects, three were binned with a hair density of 1.8 hairs/mm<sup>2</sup>, four with 2.2 hairs/mm<sup>2</sup>, and eight with 2.8 hairs/mm<sup>2</sup>. Both of the bald subjects had hair root densities in the 1.8 hairs/mm<sup>2</sup> range. For the subjects measured, there was no obvious correlation between hair density and hair color. The long hair subjects had hair lengths in the 220–420 mm range while the short hair subjects had lengths in the 0–30 mm range. All four long haired subjects had hair densities in the 2.8 hairs/mm<sup>2</sup> category. All subjects were right handed and had one repeated measurement within 2–3 weeks of their first visit. None of the subjects had dyed hair or had used any cosmetic hair products when fNIRS measurements were done. The studies were performed under the approval of the University of Texas at Arlington Institutional Review Board protocol (IRB No.: 2011-0193).

#### 2.1.2. The fNIRS experimental setup

The brush optodes (Fig. 1) were used as extensions that were attached to the flat end tips of the flat-faced optodes of a commercially available fNIRS system (CW-6, Techen Inc., Milford, Massachusetts). The individual fibers in the brush optodes were made of a low-cost polymethyl methacrylate polymer (TheFiberOpticsStore.com, North Oaks, Minnesota), and had a numerical aperture (NA) of 0.41 in air. Each fiber was 0.25 mm in diameter, and 64 of them were included to form a 3 mm diameter optode [Fig. 1(a)], which could expand up to about 4 mm in diameter when threaded through hair [Fig. 1(b)]. Each bundle of brush fibers

was placed into a cylindrical envelope of black cladding to prevent ambient light from overwhelming the detected signal, exposing only 3 mm from the fiber tips. The distal end of the attachment was polished flat and was encased in a holder [Fig. 1(c)] that enabled abutting the commercial system's flat-faced fiber bundles face-on against the brush optode extensions. In prior work, we have shown through MC simulations that the expansion of the brush optode diameter due to threading through hair did not significantly affect the spatial resolution in the resulting reconstructed images, while tissue simulating phantom experiments indicated a loss of  $-2.54 \pm 1.53$  dB due to imperfect optical coupling between the brush fiber optode attachments and the flat-faced fiber bundles [22]. These attachments were secured in place with a rubber band. The holder attachments were made from acrylonitrile butadiene styrene (ABS) at low cost using a 3D printer (Stratasys, Eden Prairie, Minnesota). In comparison to the brush optodes, the commercial system's flat-ended fiber bundle optodes consisted of glass fibers, had an NA of 0.44 in air, and were 3 mm in diameter.

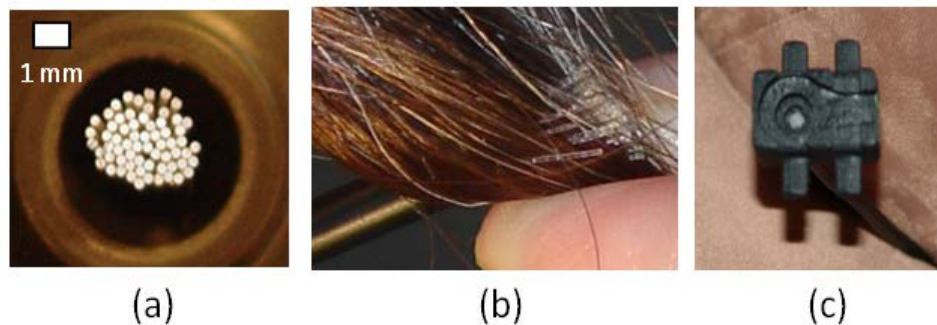


Fig. 1. Pictures of the brush-fiber optode showing (a) the brush-fiber end to be placed on an individual's head, (b) how the brush optode fibers could thread through hair to attain improved optical contact, and (c) the distal end of the brush optode that was designed to attach onto the commercial system's flat-ended fiber bundles.

fNIRS measurements of the sensorimotor cortex during finger tapping were performed with and without use of the brush optode attachments so that comparisons could be made in the quality of the resulting fNIRS signals and images. In these measurements, 12 laser sources emitted light at 830 nm and 12 at 690 nm, such that each of the source optical fiber bundles carried both wavelengths of light at each source location simultaneously. In the CW-6 system, the source fiber bundles were of 0.25 mm diameter as they consisted of only two single-mode fibers, one for each of the two illumination wavelengths. These source fibers were thin enough to easily thread through hair and be placed in contact with the scalp. The brush optode attachments were applied to the 3 mm diameter detector fiber bundles only. There were a total of 24 detectors arranged in parallel rows (Fig. 2) such that the first (1.5 cm), second (2.12 cm), and third (3.35 cm) nearest neighbor detectors were used to detect the reflected light from the respective neighboring sources. This layout resulted in a total of 112 total source-detector pairs. The source and detector fiber bundles were firmly attached onto a subject's head by Velcro straps. Since the weight of the flat optodes at the distal end of brush optode attachments pulled the brush optodes off the scalp, the brush optodes were placed in-between slits formed in a piece of airtex foam to keep the brush optodes upright so as to stabilize their placement on the scalp.

The fNIRS probe placement was such that the mid-right edge of the probe holder was 2 cm to the left of the Cz position of the EEG International 10/20 system (Fig. 2) [1]. Since activation had been located between 2 cm and 7 cm to the left of the center of the head [11], this placement enabled monitoring of activation in the contralateral primary sensorimotor region of the cortex due to right hand finger tapping. Activation at different locations within the probes' field of view (FOV, 10.5 x 6 cm) was monitored simultaneously by all source-detector pairs, as the CW-6 system enabled all lasers to be on at the same time by

multiplexing them with distinct modulation frequencies (6.4–12.6 kHz with an increment of 200 Hz). The detected back-reflected light was demodulated and sampled at a rate of 32.5 Hz. In addition to measuring the cortical hemodynamics by optical means, the finger tapping pattern was simultaneously measured by an in-house made, capacitance-based, tapping board that produced a bi-level voltage for each tap, and the respiration of each subject was monitored by a respiration belt (Sleepmate Technologies, Glen Burnie, Maryland). These measurements were fed into the CW-6, digitized by an analog-to-digital converter, also sampled at 32.5 Hz, which resulted in a common time base for both optical and auxiliary data. The reference respiration signal was subsequently filtered out of the measured time-series activation data as described below.

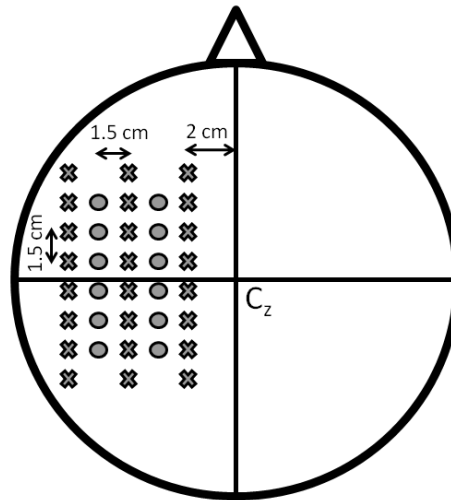


Fig. 2. Probe configuration setup on a human subject. The  $C_z$  position according to the EEG International 10/20 system and its relation to the location of the probe configuration is shown. The filled 'X' symbols identify the locations of detectors, and the filled circles identify the locations of sources.

### 2.1.3. Subject measurements

The subjects sat up straight with their heads resting back in a quiet, dimly lit room as a PowerPoint animation on a computer screen guided them through the finger tapping protocol. No set tapping frequency was required of the subjects. Thus, the tapping frequency was self-paced, which resulted in average finger tapping rates in the 1–2 Hz range. Tapping consisted of moving all fingers of the right hand, while keeping the left hand relaxed. The subjects touched the tapping board while tapping and rested their hand on the board during the no-tapping intervals. The data acquisition protocol consisted of a 180 s baseline (no tapping), immediately followed by a series of eight consecutive epochs of 15 s of tapping and 25 s of rest, and ended with a 20 s baseline measurement, resulting in a total acquisition time of 520 s (8 min. 40 s). For each visit, a 520 s protocol was done for each one of the flat and brush optode sets. After the fNIRS measurements, the hair density and the number of hair layers blocking the optodes was estimated for each subject from hair clippings. The local hair density was measured by first cutting and then counting those hairs originating from the scalp within a 5 mm radius from five different locations within the measured FOV. The average value counted from all five sampling locations provided an estimate of the local hair density for each subject. Cumulative results for hair densities binned in 1.8 hairs/mm<sup>2</sup>, 2.2 hairs/mm<sup>2</sup>, and 2.8 hairs/mm<sup>2</sup> categories are reported in the Subjects section. Subsequently, the number of hair layers blocking a single optode was also measured. The measurement was performed by placing a single flat optode on the scalp after combing away as many hairs as possible. A

plastic slide was placed under the hairs blocking the optode and the hairs were held down with tape and were cut. The hair sample was then carefully removed and the number of hair layers and hairs at each layer was counted with tweezers. This was repeated at 5 different locations within the measured FOV. These measurements provided an estimate of the number of hair layers blocking the optode from touching the scalp. For short haired subjects the measured number of hair layers and the linear density of hair on top of the scalp increased with hair root density as shown below (Table 1, Column 4).

Additionally, hair affected the number of brush fibers that could have proper optical contact with the scalp. Since the fibers of the brush optodes that were not blocked by hair left a short-lived indentation on each subject's scalp, the percentage of brush fibers blocked by hair was determined by counting the number of indentations caused by each brush optode. The percentage of obstructed fibers counted as a function of hair density is reported below (Table 1, Column 2). Notably, all fiber indentations of the brush optodes (64 fibers) were accounted for on the bald subjects.

#### 2.1.4. fNIRS signal filtering, identification of source-detector pairs with significant activation, and image reconstruction

In addition to detecting evoked hemodynamic changes, fNIRS is sensitive to cerebral hemodynamic fluctuations of systemic origin. Such systemic fluctuations can be caused by cardiac pulsation, respiration, and Mayer waves [24,25]. For typical motor activation protocols, the cortical hemodynamic response can be found in the 0.01–0.4 Hz frequency range, while physiological artifacts, such as cardiac pulsation, can be found between 0.8 and 2.0 Hz, respiration in the 0.1–0.3 Hz range, and Mayer waves at ~0.1 Hz or lower [24,25]. Because there is a significant overlap between the frequency spectra of respiration and Mayer waves and of the hemodynamic response due to brain activity, band-pass filtering is not effective in removing such physiological artifacts. Recent studies have used time-domain systems [26], multi-distance probe geometries [27], component analysis [28], adaptive filtering [29], or some combination of these [11] to remove physiological artifacts.

This study used a combination of band-pass filtering, adaptive filtering, and component analysis to filter the fNIRS signals [11]. The first step in the signal filtering was to band-pass filter fNIRS signals from all source-detector separations and the respiration belt measurements in the 0.01 and 0.4 Hz range as this frequency window was found to contain the power spectrum of activation signals as well as that of respiration and Mayer waves. Cardiac pulsation, which was in the 1 Hz range, was filtered out of this window. Subsequently, a combination of an adaptive least mean square (LMS) filter and principal component analysis (PCA) was used to remove global fluctuations from the band-pass filtered fNIRS signals [11]. The respiration belt measurement was then used as the adaptive filter noise reference for the removal of respiration noise artifacts from the fNIRS signals as previously reported [11].

Moreover, not all flat-faced and brush fiber bundles maintained good optical contact due to motion or obstruction by hair, thus propagating noise into the reconstructed images. Noisy source-detector pairs which had a signal-to-noise ratio below a determined threshold due to hair obstruction were removed from further analysis [30]. The signal-to-noise ratio ( $SNR_{s,d}$ ) values for all source-detector pairs were determined by Eq. (1):

$$SNR_{s,d} = 10 \times \log(P_{s,d} / P_d) \quad (1)$$

where  $SNR_{s,d}$  was the detected signal-to-noise ratio value for a specific source (subscript  $s$ ) and detector (subscript  $d$ ) pair,  $P_{s,d}$  was the detected light power within the 0.01 Hz to 0.4 Hz frequency range for a specific source-detector pair after being filtered, and  $P_d$  was the detected power within the same frequency range for a dark measurement (no light source on) with the specific detector. The threshold was identified by first sorting the  $SNR_{s,d}$  of source-detector pairs into groups by their corresponding source-detector distances. Each group was then split into an original set which consisted of all the  $SNR_{s,d}$  values for that group, and a pruned set

which initially consisted of the original set minus the smallest  $\text{SNR}_{s,d}$  value for that group. If the mean or standard deviation of the pruned set and original set were not significantly different ( $p < 0.05$ ), as determined by the T-test and F-test respectively, then the smallest  $\text{SNR}_{s,d}$  value was removed from the data set being pruned, and the procedure was repeated until the pruned group's mean or standard deviation was significantly different ( $p < 0.05$ ) from the original set. The last  $\text{SNR}_{s,d}$  value removed was saved as a threshold candidate. The process was repeated for each group of source-detector pair distances, and the minimum value among the saved  $\text{SNR}_{s,d}$  threshold candidates was the applied threshold for the whole data set. The source-detector pairs below the threshold that were removed for the flat optodes ( $4.57 \pm 0.77$  dB) and brush optodes ( $5.73 \pm 0.85$  dB) were shown to have significantly smaller  $\text{SNR}_{s,d}$  values than those of the flat optode ( $28.31 \pm 2.93$  dB) and brush optode ( $34.78 \pm 3.64$  dB) source-detector pairs kept for analysis. Furthermore, head movements were noted as each subject performed the protocol. Those 40-s tapping-rest intervals which contained head movements were removed from further analysis.

Reconstruction and visualization of fNIRS activation images resulting from the acquired reflectance data that passed the  $\text{SNR}_{s,d}$  selection criteria described above was performed by the open-source HomER software implemented in MATLAB [31]. In this software activation images are reconstructed by use of the Tikhonov perturbation solution to the photon diffusion equation [32,33], which employs a regularized Moore-Penrose inversion scheme [32,33]. The reconstructed, two-dimensional images (21 x 21 pixels) represented maps of  $\Delta\text{Hb}$  and  $\Delta\text{HbO}$  on the cortical surface, within the detector's FOV (Fig. 2). Images were reconstructed for every 0.03 s time interval. After the fNIRS images were reconstructed, regions of activation were determined by a general linear model (GLM) and the T-test in an approach similarly used in fMRI image analysis [34]. The GLM treats an entire time-series of a single pixel as a linear combination of model functions plus noise which are defined in a model matrix. In this case the model matrix contained a sum of gamma functions convolved with a box function to model the hemodynamic response due to finger tapping [35], and a DC component to represent the background hemodynamic fluctuations [34]. From the estimated amplitudes and estimated error variance, a T-value and a p-value was calculated for each pixel. This process was repeated for the time-series data of each image pixel. With the application of the Bonferroni corrections for multiple comparisons [36], a pixel with  $p < 0.0001$  was considered to have significant cortical activity due to finger tapping. The  $\Delta\text{HbO}$  and  $\Delta\text{Hb}$  activation images were then created from the calculated activation amplitudes for each pixel.

In addition to identifying regions of significant activation in the reconstructed images, similar analyses were performed at the detector level for both flat-faced and brush optode measurements. Using the GLM, the T-test, and the Bonferroni correction for multiple comparisons, source-detector pairs with significant activation ( $p < 0.0001$ ) were identified in each measurement data set.

#### 2.1.5. Detected signal and image metrics

fNIRS signal and image metrics were used to quantify any improvements occurring when using the brush optodes versus the commercial flat-ended fiber bundles. An activation SNR metric for fNIRS signals at the detector level was computed for the source-detector pairs that had significant activation. The activation SNR was defined for a specified source-detector pair [Eq. (2)] as the ratio of  $\beta$  to  $\sigma$ , i.e. the amplitude of the hemodynamic response as found from the GLM applied on the individual detector time-series data [34] divided by the standard deviation of the detected baseline hemodynamic fluctuation signal. It is important to note that the  $\text{SNR}_{s,d}$  defined in Eq. (1) is different from the SNR defined in Eq. (2). SNR will refer to the activation SNR [Eq. (2)] from this point onward. After creating the activation images and determining the regions of activation by use of the aforementioned GLM and T-test on each image pixel, the CBR of the activation images was found with Eq. (3). In that equation  $\mu_A$  was the mean value of the activation regions,  $\mu_B$  was the mean value of the background regions, and  $\sigma_B$  was the standard deviation of the background region values.



$$\text{SNR} = 10 \times \log(\beta / \sigma) \quad (2)$$

$$\text{CBR} = (\mu_A - \mu_B) / \sigma_B \quad (3)$$

Additionally the dAoA was determined by the summation of the pixel areas with activation.

#### 2.1.6. Statistical analysis

One-sampled T-tests or Wilcoxon Signed-Rank tests were performed, using SAS 9.1 (SAS Institute Inc., Cary, North Carolina) to see if there was a significant difference ( $p < 0.05$ ) in SNR, CBR, and dAoA means between visits and between the use of the flat and brush optodes. Prior to testing the significant difference of the means between groups, the F-test was used to assess if the variances of both groups being tested were significantly different from one another. In cases where the variance of flat-faced versus brush optode measurements was found to be significantly different ( $p < 0.05$ ), the Wilcoxon Signed-Rank test was used instead. Such instances occurred when comparing the CBR and dAoA for the overall comparison of the  $\Delta\text{Hb}$  and  $\Delta\text{HbO}$  data in subjects with black hair and in subjects with the higher hair densities of 2.2 and 2.8 hairs/mm<sup>2</sup>. All other cases used the T-test to compare between group means. The null hypothesis was defined as a zero change between visits or between uses of the two different optode sets.

#### 2.2. Monte Carlo simulation of photon transport through hair and scalp tissue

The transport of NIR light through layers of hair and the scalp, which contained hair roots, was modeled for different hair colors and densities by MC simulation software (FRED, Photon Engineering LLC, Tucson, AZ). The purpose of these simulations was to obtain estimates of the attenuation NIR light experienced from the point it entered the scalp to the point it was collected by an optode.

NIR photon transport, at an assumed wavelength of 830 nm, was simulated for hair laying on top of a block of scalp tissue [10 x 10 x 4 mm<sup>3</sup> (length x width x height)] embedded with hair follicles (Fig. 3). Photons were injected from the bottom side of this tissue block by a virtual source at half angles of 0° to 90°, mimicking the fact that the angular distribution of photons arriving there after having traveled deeper in the brain would be isotropic. To emulate a detection fiber bundle, a virtual optode was placed on top of the hair and was simulated to collect light within a cone of 18° half-angle to match the NA of these fibers in air. For the case of flat-faced fiber optodes, a virtual detector [Fig. 3(a), blue circle] was placed on top of the highest hair layer and was simulated as a pure absorber of photons with a 3 mm diameter circular aperture to emulate the fiber bundles used for the human measurements. Similarly, a brush fiber optode was simulated to consist of 64 individual fibers of 0.25 mm circular aperture each, placed with an inter-fiber center to center spacing of 0.375 mm with all fibers being contained within a circle of 4 mm diameter. In the case of the brush optodes, only a certain percentage of the brush fibers was blocked by hair while the rest had good optical contact with the scalp. Examples of a single brush fiber that is blocked and of one that is not blocked by hair are shown in Fig. 3(b) as the short and the long blue cylinders, respectively. The percentage of obstructed fibers assumed in the brush optode simulations as a function of hair density were measured experimentally (see Subject Measurements section) and are reported below (Table 1, Column 2). MC simulations were performed for hair densities spanning the range of measured values (0, 1.8, 2.2, and 2.8 hairs/mm<sup>2</sup>).

Several simplifying assumptions were made to make these MC simulations more tractable:

(1) To increase the photon scoring efficiency at the optodes, the source of light, mimicking the light exiting the skull, at the bottom of the 4 mm thick block of scalp tissue containing the hair roots, was shrunk from the entire bottom area (10 mm x 10 mm surface) to a 3 mm diameter source. This was done after simulating the detected photon fraction for successively smaller source diameters while verifying that the detected photon fraction remained statistically unchanged.

(2) Since this MC simulation did not track photons throughout the entire head volume, any contributions of photons coming from the sides of the modeled tissue volume were not taken into account. More specifically, the bottom and sides of the scalp tissue block were made completely absorbing, which precluded contributions to the scored photon count from photons exiting and reentering this tissue volume. However, the sides of the tissue block were several mean free paths away from both source and detector and the probability of a photon reentering the tissue volume and hitting the detector was small. This assumption was verified by running the same simulations with reflective boundaries, as opposed to completely absorbing ones, and the scored photon counts remained statistically unchanged.

(3) Since the subjects in this study had fair skin complexion, it was assumed that all of them had the same skin absorption and scattering properties. Thus, the optical properties used for the scalp tissue block for all simulations were assumed as  $n = 1.53$ ,  $\mu_a = 0.06 \text{ mm}^{-1}$ ,  $\mu'_s = 1.0 \text{ mm}^{-1}$ , and  $g = 0.9$  (to fit a Henyey-Greenstein model of scattering) [37].

(4) The scalp tissue block included evenly spaced hair follicles which were modeled as 0.1 mm diameter rods vertically extending from the air-tissue interface to 4 mm deep into the scalp tissue [38]. The number of hair follicles varied for each simulation depending on the hair density (hairs/mm<sup>2</sup>) being simulated.

(5) In the simulations the hairs were arranged parallel to each other for layers laying on top of the scalp and were perpendicular when inside the scalp. This distribution of hairs [Fig. 3(b), brown rods] was an approximation for the fact that hair sprouted vertically out of the scalp and then bended sideways so that hairs were running parallel to it. The hairs were modeled as 0.1 mm diameter rods [23] with lengths of 20 mm, representing the average hair length of a person with short hair.

(6) The average number of hair layers measured for subjects with short hair (Table 1, Column 4) were modeled in each simulation such that each layer was parallel to one another while staggered in the XY plane. Each layer was assigned 3 hairs/mm to 7 hairs/mm, depending on hair density (Table 1, Column 4), following the experimental estimates described in the Subject Measurements section. The model of a bald subject only included the hair roots within the scalp.

(7) Hair colors including blonde, brown, and black were modeled with similar scattering properties ( $\mu'_s = 0.023 \text{ mm}^{-1}$ ), yet different absorption properties ( $\mu_a = 0.01, 0.98, \text{ and } 5.82 \text{ mm}^{-1}$  respectively) based on values reported in the literature for both the hair follicles and

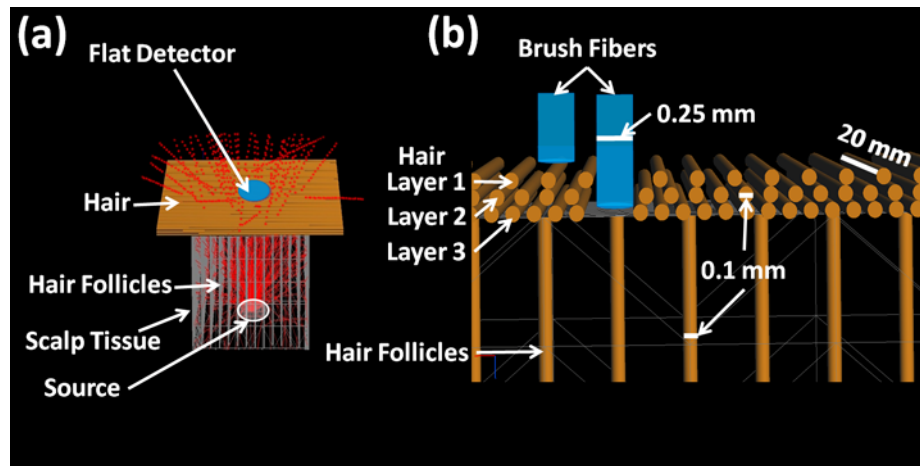


Fig. 3. Schematics of (a) the overall MC simulation setup, and (b) a zoomed-in view of the hair layers, hair follicles, and the placement of a couple of brush fibers among the 64 brush fibers used in the simulations. In (a), the red solid lines are the simulated rays inside the scalp tissue ( $10 \times 10 \times 4 \text{ mm}^3$ ), becoming red dashed lines once they left the scalp tissue. In (b), the short light blue cylinder indicates a brush fiber blocked by hair, and the long light blue cylinder a brush fiber that had good optical contact with the scalp.

hair layers [39]. The bald subjects in this study originally had black hair and thus the MC simulations modeled bald subjects having hair follicles with the absorption properties of black hair.

### 2.3. Analytical model of photon transport through hair and scalp tissue

The attenuation that NIR light experienced due to scalp tissue and hair was also estimated analytically for subjects with short hair both for brush fiber and flat-faced optodes.

For the brush fiber optodes the analytical equation estimating the fraction of NIR light reaching a detector fiber after exiting the scalp [ $R_d$ , Eq. (4)] considered the detected reflectance of NIR light for both obstructed and unobstructed fibers, the absorption of NIR light through the hair layers on top of the scalp, the fraction of brush fibers obstructed by hair, and the light collection efficiency of an obstructed fiber:

$$R_d = (1 - OF) \times R_{T,NObs} + OF \times D_{Eff} \times R_{T,Obs} \times \exp(-\mu_{a^*,H} \times z) \quad (4)$$

The first term on the right hand side of Eq. (4) estimated the detected reflectance from the fraction of fibers which had good optical contact with the scalp, whereas the second term estimated the detected reflectance for the fraction of fibers obstructed by hair. The summation of these two terms resulted in the fraction of light traveling through the scalp that reaches the detector,  $R_d$ . If the fraction of brush fibers obstructed by hair ( $OF$ ) was equal to zero ( $OF = 0$ , e.g. a bald subject) then only the first term on the right hand side of the equation would remain. However, as  $OF \rightarrow 1$ , the second term became dominant. The  $OF$  was estimated from experimental measurements for each measured hair density (Subject Measurements section and Table 1). Additionally, in Eq. (4)  $R_{T,NObs}$  is the reflectance of light at the scalp-air interface when an individual fiber had good optical contact with the scalp,  $R_{T,Obs}$  is the detected reflectance when an individual fiber was obstructed by hair,  $\mu_{a^*,H}$  is the volume-averaged absorption coefficient of the hair layers,  $z$  is the distance from the surface of the scalp to the obstructed fiber, and  $D_{Eff}$  is the reduction in geometric collection efficiency of the obstructed fiber in comparison to an unobstructed fiber.

Several simplifying assumptions were made when calculating  $R_d$ :

(1) The light reflecting at the scalp-air interface was treated as a plane wave and the potential gradient of the reflectance profile across the face of the detector optode was ignored to simplify the calculations. In comparison to how the MC simulations were performed (Fig. 3), the diffuse plane wave reaching a depth of one mean free path away from the scalp-air interface was considered as the source term. This source term was propagated through the scalp-air interface using the reflectance model given by Eq. (5), where  $R_T$  is the diffuse plane wave reflectance at this tissue-air interface,  $A$  is a proportionality constant (Eq. (6)),  $\mu_{tr} = (\mu_a + \mu'_s)$  is the transport coefficient,  $a' = \mu'_s / \mu_{tr}$  is the reduced albedo, and  $\mu_{eff} = \sqrt{3\mu_a\mu_{tr}}$  [40]. As in this diffusion model the source term is non-directional, the original incoming direction of the plane wave, whether from the top of the scalp or from below the scalp, did not change the reflectance model used in Eq. (5):

$$R_T = \frac{3Aa'}{[(\frac{\mu_{eff}}{\mu_{tr}} + 1)(\frac{\mu_{eff}}{\mu_{tr}} + 3A)]} \quad (5)$$

$$A = \frac{1 - R_{eff}}{2(1 + R_{eff})} \quad (6)$$

(2) As shown in Eq. (6), the proportionality constant is dependent on the effective reflectance coefficient ( $R_{eff}$ ). Therefore, the value of  $A$  differs between fibers with good optical contact with the scalp and those obstructed by hair. Given that light travelling through the scalp propagates mostly in the forward direction, as seen in Fig. 3(a), the simplifying assumption is made to ignore the spatial variability in refractive index matching conditions

between scalp regions touched by a fiber and ones that are not. Instead, it assumed that the matched boundary condition applies for the diffuse planar wave solution shown in Eq. (5) when a fiber touches the scalp, whereas a scalp-air boundary condition applies for fibers obstructed by hair. A mismatch in the index of refraction ( $n$ ) between the scalp tissue and air causes a change in  $R_{eff}$  [41]. Typically, the index of refraction for tissue is  $n = 1.4$  and  $R_{eff}$  for a tissue-air interface is 0.493 [39]. However, since this study is concerned with the attenuation due to scalp tissue, the index of refraction for the scalp ( $n = 1.53$ ) [35] is used instead and the  $R_{eff}$  is recalculated to be 0.614 when a fiber is obstructed by hair [41]. When an optical fiber has good contact with the scalp, there is no index of refraction mismatch due to the tissue-air interface and thus  $R_{eff} = 0$  [41].

(3) Since the  $\mu_a$  of hair follicles changed for different hair colors and the  $\mu'_s$  of hair follicles was different from that of scalp tissue, it was necessary to calculate volume-averaged  $\mu_a$  and  $\mu'_s$  values for a 'homogenized' scalp tissue so that Eq. (5) could be evaluated. These effective  $\mu_a$  and  $\mu'_s$  values of the scalp tissue were calculated by Eq. (7):

$$\mu_{\bullet, HF} = VF_{HF} \times \mu_{\bullet, HF} + (1 - VF_{HF}) \times \mu_{\bullet, T} \quad (7)$$

represented the  $\mu_a$  or  $\mu'_s$  values (the dot subscript indicates either one) weighted by the volume fraction ( $VF_{HF}$ ) of hair follicles (subscript  $HF$ ) in the scalp (Table 1, Columns 5-8). Furthermore the volume fraction of hair follicles within scalp tissue was calculated by Eq. (8), where  $HD$  was the hair density,  $A_T$  the cross-sectional area of the scalp tissue,  $V_T$  the volume of the scalp tissue, and  $V_{HF}$  the volume of an individual hair follicle:

$$VF_{HF} = \frac{HD \times A_T \times V_{HF}}{V_T} = HD \times A_{HF} \quad (8)$$

Since the thickness of scalp tissue and the length of a hair follicle are assumed to be the same, this equation can be simplified so that  $VF_{HF}$  is found by the hair density and cross-sectional area of a hair follicle ( $A_{HF}$ ). Moreover,  $\mu_{eff}$ ,  $\mu_{tr}$ , and  $a'$  must be recalculated with  $\mu_{a, HF}$  and  $\mu'_{s, HF}$  before calculating  $R_{T, Obs}$  and  $R_{T, Obs}$ .

(4) Similarly, the volume averaged  $\mu_a$  and  $\mu'_s$  of the hair layers surrounded by air would change due to hair color and hair density. In Eq. (9),  $\mu_{\bullet, H}$  is the volume-averaged  $\mu_a$  or  $\mu'_s$  of the hair layers (Table 1, Columns 5-8),  $VF_H$  is the volume fraction of the hair layers between the scalp and the optode (Table 1, Column 3), and  $\mu_{\bullet, H}$  is the  $\mu_a$  or  $\mu'_s$  of the hair.

$$\mu_{\bullet, H} = VF_H \times \mu_{\bullet, H} \quad (9)$$

$$VF_H = \frac{H_{mm} \times L \times A_H \times D_d}{L \times D_H \times D_d} = \frac{H_{mm} \times A_H}{D_H} \quad (10)$$

Furthermore, the volume fraction was calculated by Eq. (10) where  $H_{mm}$  is the number of hairs per millimeter in each layer (Table 1, Column 4),  $A_H$  is the cross-sectional area of a hair,

**Table 1. The obstruction fraction (OF) of brush optodes, the volume fraction of the hair follicles in the scalp ( $VF_{HF}$ ) and of the hair layers between the scalp and the detector fiber ( $VF_H$ ), the linear hair density ( $H_{mm}$ ) and number of hair layers ( $L$ ), and the volume-averaged  $\mu_a$  and  $\mu'_s$  for the scalp and hair layers as a function of hair root density**

Hair Root Density (hairs/mm <sup>2</sup> )	Brush OF	$VF_{HF} / VF_H$ (no units)	$H_{mm}/L$ (hairs/mm)/(no units)	Blonde $\mu_{a, HF} / \mu_{a, H}$ (mm <sup>-1</sup> )	Brown $\mu_{a, HF} / \mu_{a, H}$ (mm <sup>-1</sup> )	Black $\mu_{a, HF} / \mu_{a, H}$ (mm <sup>-1</sup> )	$\mu'_{s, HF} / \mu'_{s, H}$ (mm <sup>-1</sup> )
<b>0 (Bald)</b>	0	0.01/0.00	0/0 layers	0.06/—	0.07/—	0.14/—	0.986/—
<b>1.8</b>	0.20	0.01/0.24	3/3	0.06/0.002	0.07/0.23	0.14/1.37	0.986/0.05
<b>2.2</b>	0.60	0.02/0.39	5/3	0.06/0.003	0.08/0.38	0.16/2.29	0.983/0.09
<b>2.8</b>	0.90	0.02/0.55	7/3	0.06/0.005	0.08/0.53	0.19/3.20	0.979 / 0.13

and  $D_d$  is the diameter of a detector fiber. The cross-sectional area of a hair was found by  $A_H = \pi(D_H/2)^2$  where  $D_H = 0.1$  mm.

(5) Since  $\mu_{s^*,H}$  was small and little refraction of light was caused by the hair layers on top of the scalp, as was confirmed by MC simulations, the attenuation of light due to the hair layers was primarily due to light absorption. The light attenuation due to the hair layers was therefore expressed by the exponential term in Eq. (4), which follows the Beer-Lambert law. The  $z$  term in Eq. (4) can be expressed as  $z = L \times D_H$ , where the number of hair layers,  $L$ , is seen in Table 1, Column 4, as a function of a subject's hair root density.

(6) The last simplification was that the geometric light collection efficiency of a brush optode was found by treating it as a group of 64 individual fibers cemented together acting as a single optode to collect the sum total of the detected intensity. Differences in the relative geometric light collection efficiency ( $D_{Eff}$ ), when the optode was lifted upwards from the scalp surface by hair, were compared to the collection efficiency achieved when the optode touched the scalp surface ( $OF = 0$ ) [42]. The collection efficiency comparison for an optode was given by Eq. (11) where  $r$  was the radius of the optode, and  $z$  the distance of this optode from the surface of the scalp.

$$D_{Eff} = 1 - \frac{z}{\sqrt{z^2 + r^2}} \quad (11)$$

Given that the radius of a brush optode expanded to 2.0 mm when threaded through hair,  $D_{Eff}$  was equal to 0.950, 0.901, 0.852 for  $z = 0.1, 0.2$ , and  $0.3$  mm, i.e.  $L = 1, 2$  and  $3$  hair layers respectively. As for a flat-faced optode with a radius of 1.5 mm,  $D_{Eff}$  was equal to 0.934, 0.868, 0.804 for  $z = 0.1, 0.2$ , and  $0.3$  mm, respectively. On the other hand when the optode was not obstructed  $D_{Eff} = 1$  ( $z = 0$  mm).

Equation (4) and all the considerations following it, as described above, were also used to calculate the percent power loss for the case of the flat-faced optodes. However, in contrast to the case of brush optodes where  $OF$  was measured experimentally (Table 1, Column 2), it was not easy to measure  $OF$  for the flat-faced optodes and an analytical estimation model was used instead:

The variation of  $OF$  for a flat-faced optode with hair density was determined by first finding the number of hairs remaining under the flat-faced optode after combing away as much hair as possible. The remaining number of hairs per millimeter after combing ( $HR$ ) had an approximate linear relationship with the hair root density ( $HRD$ ):  $HR = 10 \times HRD - 7$ , with  $HR = 0$  for  $HRD < 0.7$  hairs/mm<sup>2</sup>. Given that the maximum linear density per hair layer that could occur in adult subjects was  $H_{max} = 7$  hairs/mm [23], the number of layers was estimated by rounding down to the nearest integer  $L = \text{int}(HR / H_{max})$  and then the number of hairs per millimeter per layer remaining under the optode ( $HR_{mm}$ ) was found by  $HR_{mm} = HR / L$ . Finally, the following three cases occurred for  $OF$  depending on the deduced number of hair layers:

- (i)  $L = 0$ : The flat-faced optode was not obstructed by hair and  $OF = 0$ .
- (ii)  $L = 1$ : The flat-faced optode was partially obstructed by a fraction equal to the hair-covered area divided by the total area of this fiber bundle optode of 3 mm diameter ( $D_d$ ):

$$OF = \frac{HR_{mm} \times D_H}{\sqrt{\pi} (D_d / 2)} \quad (12)$$

- (iii)  $L > 1$ : The flat-faced optode was completely obstructed by hair and  $OF = 1$ .

When substituting the calculated  $OF$  back in Eq. (4) the obstructed fraction was assigned an air-tissue boundary condition ( $R_{eff} = 0.614$ ) and the non-obstructed fraction a matched boundary condition ( $R_{eff} = 0$ ), as appropriate for cases (i)-(iii).

The calculated brush fiber and flat-faced optode  $R_d$  values [(Eq. (4))] for different hair colors and hair densities were compared against corresponding results from MC simulations and experimental measurements as described below.

### 3. Results and discussion

#### 3.1. Experimental measurements

During placement of the flat optodes on the subjects' heads a large amount of time (35–45 min) was used in attempting to part hair so that each optode would have proper optical contact with the scalp. Parting of the hair was difficult since there was limited space due to the dense probe geometry used in this work. However, the setup time was greatly reduced (10–15 min) when using the brush optode attachments, due to the brush optodes' ability to thread through hair. The threading through hair by the brush optodes also improved the optical contact with the scalp which resulted in increased SNR, CBR and dAoA for both  $\Delta\text{HbO}$  and  $\Delta\text{Hb}$  (Fig. 4). Since the results of the  $\Delta\text{HbO}$  and  $\Delta\text{Hb}$  signals and images were similar, further analysis is presented only for  $\Delta\text{HbO}$  data. Different levels of statistical significance in Fig. 4 are represented by single ( $p < 0.05$ ), double ( $p < 0.005$ ), and triple ( $p < 0.0005$ ) asterisks, respectively.

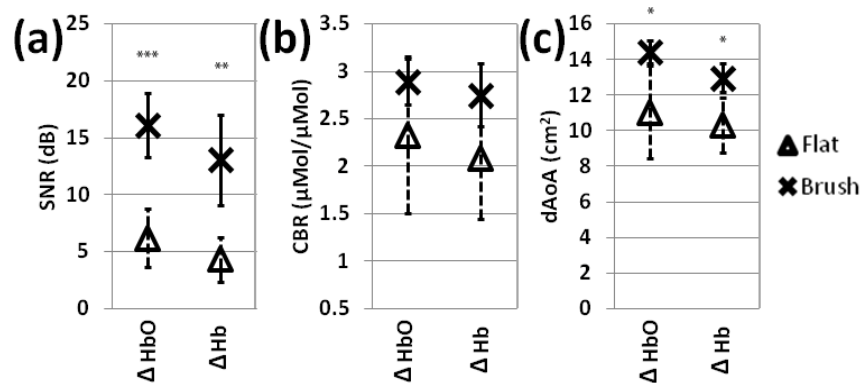


Fig. 4. A comparison of  $\Delta\text{HbO}$  and  $\Delta\text{Hb}$  (a) SNR, (b) CBR, and (c) dAoA between flat and brush optode sets. The single ( $p < 0.05$ ), double ( $p < 0.005$ ), and triple ( $p < 0.0005$ ) asterisks identify the significance in activation metric mean difference between the flat and brush optode measurements.

With a detector-to-detector comparison [Fig. 5(a)], a clearer depiction of the improved activation SNR by the brush-fiber optode was seen. In Fig. 5(a) the vast majority of the brush-fiber optodes were shown to provide a larger activation SNR than the flat optodes. Moreover, the activation SNR improvement attained when using the brush-fiber optodes was visible in the time-averaged  $\Delta\text{HbO}$  plots of subjects spanning the entire range of hair densities—examples are shown for the lowest hair density (bald) [Fig. 5(b)] and highest hair density (2.8 hairs/mm<sup>2</sup>) categories [Fig. 5(c)].

Comparing the  $\Delta\text{HbO}$  activation images [Figs. 6(a)-(b)], there was a noticeable increase in the dAoA when using the brush optodes. The pixel values in the activation images were the values of the hemodynamic response amplitude determined by the GLM described in the Methods section. To be clear, an increase in dAoA does not mean that the physical activation area grew. Rather, the existence of more source-detector pairs with low activation SNR for the higher sensitivity brush optode measurements resulted in a larger apparent area of activation in reconstructed images due to the low spatial resolution of fNIRS. Additionally, the brush optodes had significantly ( $p < 0.0005$ ) higher SNR when comparing areas in which both optode sets had detected activation [Fig. 6(c)]. It was also validated that the activation SNR improvement ( $10.12 \pm 3.17$  dB) was much larger than the activation SNR variability ( $0.59 \pm 2.63$  dB) between the two visits for each subject (difference signal =  $-8.72 \pm 7.15$  dB,

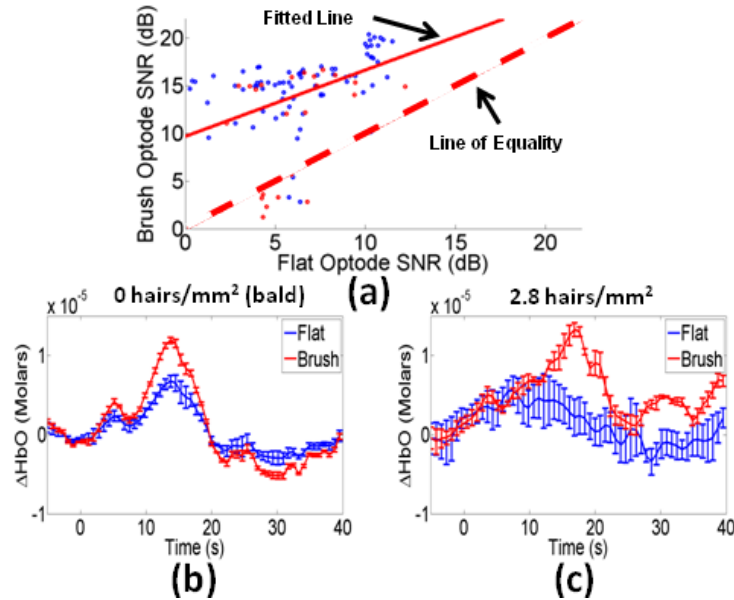


Fig. 5. (a) A scatter plot comparing the activation SNR (dB) of the flat optodes (x-axis) versus that of the brush-fiber optodes (y-axis). The blue circles (short hair subjects) and red circles (long hair subjects) are SNR data points, the red-dashed line indicates the line of equality between the two SNRs, and the red-solid line shows a linear fit through the data.  $\Delta\text{HbO}$  averaged time-plots are shown for (b) a bald subject (0 hairs/mm<sup>2</sup>) and (c) a subject with 2.8 hairs/mm<sup>2</sup>.

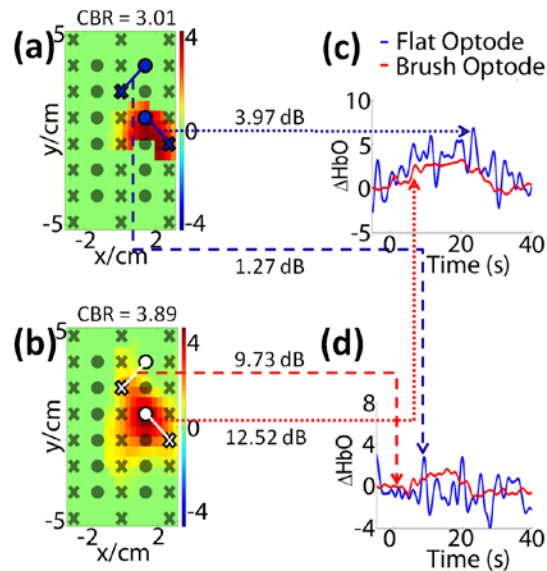


Fig. 6.  $\Delta\text{HbO}$  activation images ( $\mu\text{Molar}$  scale) for the same subject (black hair at a density of 2.2 hairs/mm<sup>2</sup>) using (a) the flat optodes and (b) the brush optodes. The sources (grey filled circles) and detectors (grey filled Xs) are used to show the source and detector locations. (c) In regions where activation could be detected by both the flat and brush optodes, the latter resulted in significantly higher SNR (shown in dB). There were also locations where the flat optodes detected no significant activation where the brush optodes did (d).

$p = 0.0073$ ). Furthermore, low amplitude activation regions were detected with the brush optodes that were not detected with the flat optodes, due to poor optical contact [Fig. 6(d)].

Also, the success rate of effectively measuring a subject on both visits with the flat optodes amongst short haired subjects was 84.62% (11/13) and 25% (1/4) amongst long haired subjects whereas the brush optodes had a success rate of 100% (13/13) and 75% (3/4), respectively.

Since darker hair absorbs more NIR light [39], it was hypothesized that the SNR would decrease with darker hair colors, due to the reduced number of photons reaching the detectors. Looking at individual subjects measured with similar hair lengths (20–23 mm, except for the bald subject) and hair densities ( $\sim 2.8$  hairs/mm<sup>2</sup>) but different hair colors, the dAoA was smaller for subjects with darker hair colors for the flat optodes (Fig. 7) due to the decreased SNR [Fig. 8(a)]. Additionally, the brush optodes successfully detected activation from the subject with black hair whereas the flat optodes failed (Fig. 7). Head curvature also had an effect on the optical contact as demonstrated by the difference in dAoA (Fig. 7) and SNR [Fig. 8(a)] between the two optode sets for the bald subject. Due to the dense geometry used, the probe set had difficulty bending along the curvature of the head when using the flat optodes causing the flat optodes at the edges of the FOV to face at an angle to the scalp. Since the brush optode fibers bended and expanded at the brush end, they were able to keep good contact with the scalp along the curvature of the head.

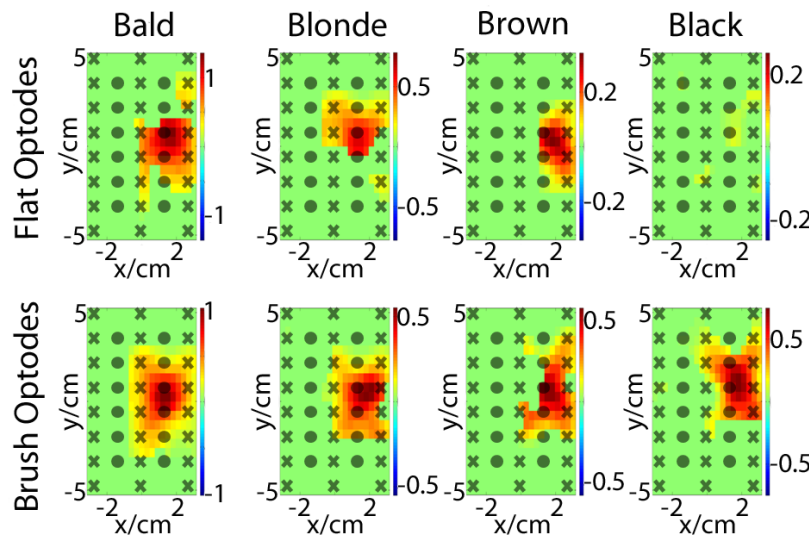


Fig. 7.  $\Delta$ HbO activation images, with color scales in  $\mu$ Molar, for four individual subjects with similar hair densities ( $\sim 2.8$  hairs/mm<sup>2</sup>) and hair lengths (20–23 mm), but different hair colors. Source positions are identified by the grey filled circles and the detector positions by the grey filled Xs.

An overall comparison of the SNR, CBR, and dAoA over different hair colors is presented in Fig. 8 separately for short haired [Figs. 8(a)-(c)] and long haired [Figs. 8(d)-(f)] subjects. Similar to Fig. 4, the statistical significance in Fig. 8 is presented by asterisks. As indicated in Fig. 8(a) there was a statistically significant ( $p < 0.05$ ) improvement in the SNR when using the brush optodes for all hair colors. Hair color did have an effect though, which was seen by the downward trend in SNR for darker hair for both sets of optodes. Despite the gains in SNR, the CBR only had small improvements ( $p < 0.05$ , statistical power ( $1 - \beta$ ) = 0.82) for blonde and brown hair color subjects [Fig. 8(b)]. The small changes in CBR can be explained by Eq. (3) which presents the CBR dependence on the mean activation amplitude and the standard deviation of the background pixel values in the activation images. In the case where many source-detector pairs had good SNR weak activation areas were detected. Inclusion of lower amplitudes in the numerator of Eq. (3) combined with no significant changes in the denominator resulted in lowering the overall CBR. On the other hand, in the case where more source-detector pairs had lower SNR, activation regions appeared more localized because



lower activation amplitude pixels were lost in the hemodynamic background fluctuations. Therefore, the mean activation amplitude was higher in the numerator of Eq. (3), but the standard deviation of the background pixels was also higher, due to increased noise, in the denominator. In the end, due to this interplay between signal amplitude and background noise the CBR in images obtained from the brush or the flat-faced optodes was similar. Finally, the brush optodes had a greater dAoA than the flat-faced optodes for all short haired subjects [Fig. 8(c)], as was also discussed for a sample case in Fig. 6 above.

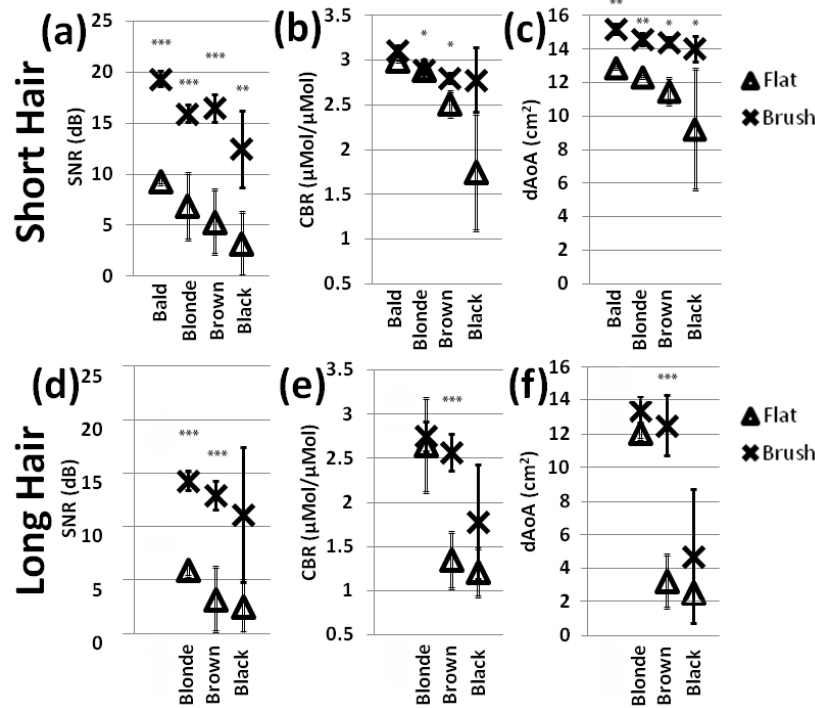


Fig. 8. Scatter plots comparing the  $\Delta\text{HbO}$  trend in (a) SNR, (b) CBR, and (c) dAoA for all short hair subjects ( $n = 13$ ) for both the flat optodes ( $\Delta$ ) and brush optodes (X). Similar plots were made for long hair subjects ( $n = 4$ ) (d)-(f). The single ( $p < 0.05$ ), double ( $p < 0.005$ ), and triple ( $p < 0.0005$ ) asterisks identify the significance in activation metric mean difference between the flat and brush optode measurements.

As for the long haired subjects [Figs. 8(d)-(f)], the SNR at the detector level was found to be greatly improved for all hair colors [Fig. 8(d)]. However, the trends in CBR [Fig. 8(e)] and dAoA [Fig. 8(f)] were not as consistent for the long haired subjects, indicating greater improvements for the brown hair subjects at least. Nevertheless, this was only a result of a current shortcoming of the brush optodes used in this work and is not a fundamental limitation: It was observed that in the long haired subjects, the brush fibers could not reach the scalp because their length was too short to thread through all the hair layers. In that detection geometry, the black hair would be more absorbing and therefore contribute to significantly higher signal attenuation, as was observed in the measurements. This problem could be alleviated in future work by constructing and using longer brush fiber optodes for the longer hair subjects so that the scalp can be reached more easily.

After examining the effect of hair color on fNIRS images, the effect of hair density on these images was also analyzed (Fig. 9). Images obtained using the brush and flat optodes were compared for individual subjects with black hair and similar hair lengths (20–23 mm, except for the bald subject), but different hair densities. As can be seen in Fig. 9, subjects with denser hair had less dAoA, which was explained by the statistically significant ( $p < 0.05$ ) lower SNR [Fig. 10(a)] at higher hair densities. Typical images from individual subjects in

each hair density category are presented in Fig. 9, whereas group average results are presented in Fig. 10. Long hair subjects were not compared across hair densities, since all these subjects had a similar hair density of  $\sim 2.8$  hairs/mm<sup>2</sup>. As was also observed when comparing results for different hair colors in Fig. 8 above, when plotting results as a function of hair density, one can see gains in SNR [Fig. 10(a)] and dAoA [Fig. 10(c)], but no significant gains in CBR [Fig. 10(b)]. Furthermore, when using the brush optodes, the dAoA values across all hair densities were similar to the values found for bald subjects [Fig. 10(c)].

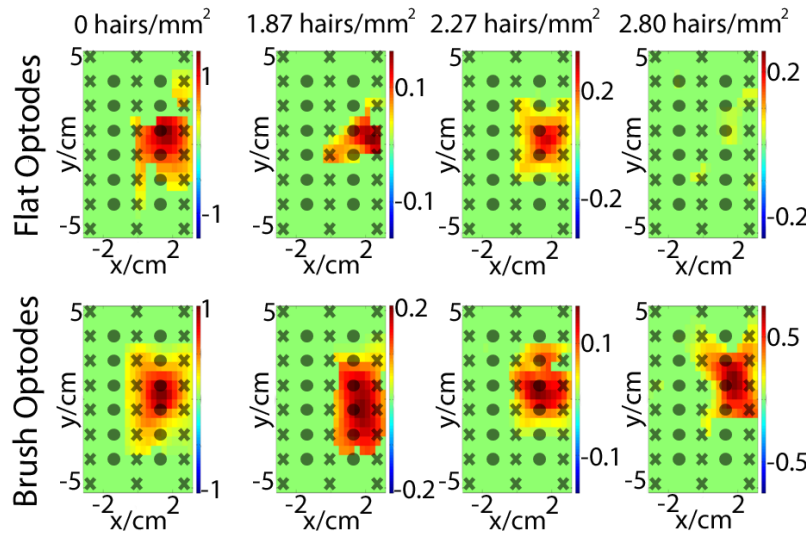


Fig. 9.  $\Delta\text{HbO}$  activation images (color scales in  $\mu\text{Molar}$ ) for four individual subjects with similar hair color (black), but different hair densities for both flat and brush optode sets. Source positions are identified by the grey filled circles and the detector positions by the grey filled Xs.

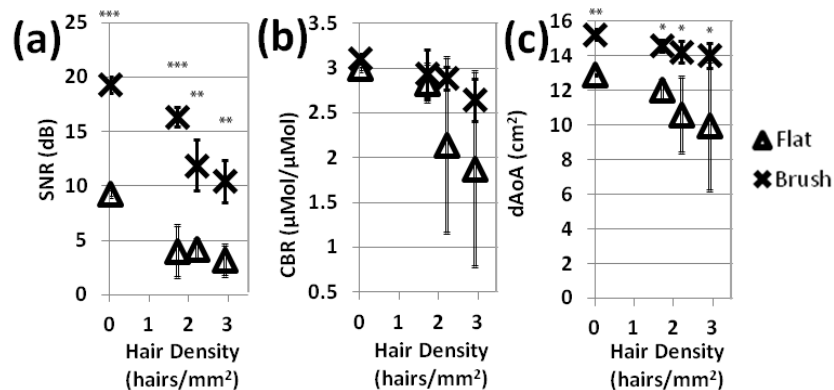


Fig. 10. Scatter plot comparing the  $\Delta\text{HbO}$  trend in (a) SNR, (b) CBR, and (c) dAoA for short hair subjects of all hair colors ( $n = 13$ ) for both the flat optodes ( $\Delta$ ) and brush optodes (X). The single ( $p < 0.05$ ), double ( $p < 0.005$ ), and triple ( $p < 0.0005$ ) asterisks identify the significance in activation metric mean difference between the flat and brush optode measurements.

### 3.2. Comparison of fNIRS signal attenuation measurements with corresponding Monte Carlo simulation and analytical model estimates

MC simulations using the FRED software and an analytical formula [Eq. (4)] were used to estimate the magnitude of fractional light power attenuation for different hair densities and hair colors for comparison against the human subject measurements. Not only did the MC

results approximate the experimentally measured power losses well but, fascinatingly, the derived analytical model predictions were found to be within a few percent of both the MC simulation and experimental results, as shown in Fig. 11 below, despite many simplifying assumptions. In addition, the diffusion theory based calculation of NIR light transport through the scalp [Eq. (5)] was compared against Kubelka-Munk theory [43,44] and results were found to be very similar for all hair colors and densities (data not shown). This comparison indicated that the diffusion approximation was not violated even for subjects with dense dark hair, which was most likely due to the volume averaging of the high  $\mu_a$  values of hair with the lower  $\mu_a$  of the surrounding scalp in this 'homogenized' scalp tissue model. In this work a large number of long haired subjects were not recruited and thus a detailed comparison with the MC simulations and analytical formula was not performed for these subjects.

In Fig. 11 the experimental results for the percent power loss in a short haired subject with respect to a bald subject were compared to corresponding MC simulations and analytical model calculations for different hair colors. Since hair densities varied within each group of hair colors, the results displayed in Fig. 11 plot the percent power loss across the different hair densities encountered in this work (0–2.8 hairs/mm<sup>2</sup>) separately for each hair color. Though for the subject pool recruited in this work no non-bald subjects existed with low hair densities, an additional hair density of 1.0 hairs/mm<sup>2</sup> was included into Fig. 11 for the MC data to estimate the trend between hair densities of 0 and 1.8 hairs/mm<sup>2</sup> for completeness. Also, additional hair densities were included between 0 - 2.8 hairs/mm<sup>2</sup> in the evaluation of the analytical model so as to produce smooth continuous curves. In these calculations the *OF* of the brush optodes for hair densities in-between the values listed in Table 1 were linearly interpolated from the experimental measurements for each hair density. Examining Fig. 11 across each row, it is apparent that darker hair colors caused an increase in the percent power loss. The percent power loss for the flat optodes had shallow slopes with increasing hair density that reflected the linear dependence of volume-averaged light absorption on the volume fraction of hair roots and hair [Eqs. (8) and (10)]. These power loss slopes as a function of hair density were steeper for the darker hair colors. On the other hand, in Fig. 11 it is apparent that the percent power loss was reduced when using the brush optodes for all hair colors though less so at the higher hair densities.

The slope of power loss in each graph comprising Fig. 11 had three stages as a function of hair density. In the first low hair density stage (approx. 0–1 hairs/mm<sup>2</sup>) the percent power loss slope was close to zero as both flat-faced and brush optodes had good optical contact with the scalp. Nevertheless, some power loss started becoming noticeable for the flat-faced optodes above 0.7 hairs/mm<sup>2</sup>, as the optodes were partly lifted off the scalp by the hair below them. In contrast, the brush optodes kept good optical contact with the scalp because they could fit between the hairs. In the second stage of the graphs in Fig. 11 (approx. 1–2 hairs/mm<sup>2</sup>) there was a larger power loss slope. The brush optodes had a shallower slope than the flat-faced optodes, because some of the brush fibers always attained matched boundary conditions with the scalp. In contrast, the large jump in power percent loss seen in the second stage for the flat-faced optodes occurred because these were now almost completely lifted off the scalp by the hair underneath them that could not be removed and  $R_{\text{eff}}$  changed from matched ( $R_{\text{eff}} = 0$ ) to air-tissue boundary conditions ( $R_{\text{eff}} = 0.614$ ). In the third stage (approx. 2–3 hairs/mm<sup>2</sup>) the slope of the graphs changed again. In this stage, the flat-faced fibers were completely lifted off the scalp and increasing the hair density only increased the Beer-Lambert attenuation (Eq. (4), second term). In contrast, the brush fibers had a larger percent power loss slope in this third stage. This occurred because the space between brush fibers was now getting filled by hair and a bigger fraction of brush fibers was being lifted off the scalp by the hair accumulating underneath them as the hair root density increased. If the brush fibers used in this work were longer in length, more hair could stack in-between them, rather than below them, and therefore the transition from stage two to stage three could be pushed to even higher hair densities.

By re-plotting Fig. 11 so that the comparisons of the percent power loss were made for different hair density categories as a function of hair color (graphs not shown), an increase in

percent power loss with increasing hair density was found for all hair colors. However, in contrast to Fig. 11 where power losses had shallow slopes with linearly increasing hair density, the power loss increased sharply with darker hair color for both the flat-faced optodes and the brush fibers. These sharper slopes were primarily due to the exponential Beer-Lambert law of attenuation experienced by light traveling through the hair layers [Eq. (4)]. It should also be noted that although the recruited bald subjects only had a low hair root density and black hair roots, they were used as the reference for all plots in Fig. 11 and all other analyses. This was because finding bald subjects with different hair root colors and densities or no hair roots at all, to thus provide ideal comparison standards, was not practical.

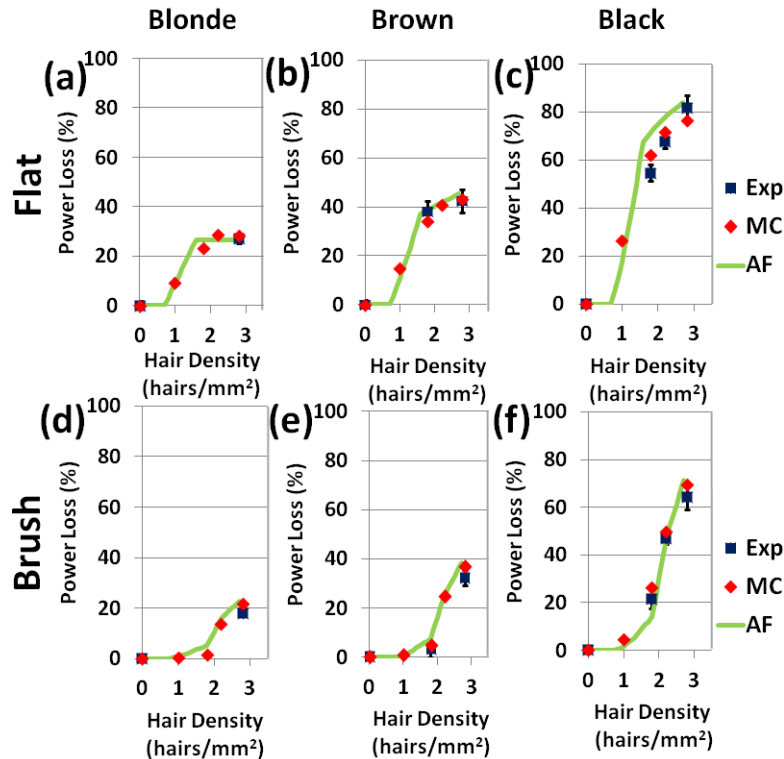


Fig. 11. The percent power loss with respect to bald subjects when using either the flat or the brush optodes. Comparison of the experimental (Exp), MC simulated (MC), and analytical formula (AF) results is performed across hair densities for each hair color.

Although significant signal gains were attained by using the brush optodes in most cases, Fig. 11 also indicates that subjects with the highest hair density only had slightly lower percent power losses compared to the corresponding flat optode measurements. By consulting the optode obstruction fraction as a function of hair density (Table 1, Column 2) one can see that obstruction of brush fibers is 90% at the highest hair density. Therefore in that case most fibers were lifted up from the scalp by hair and the collection geometry was similar to that of the flat optode. Interestingly, even though percent power losses were similar between brush optodes and flat optodes for the highest hair density category, Fig. 10(a) indicates that there were nevertheless significant gains in SNR for that category. The observation that even bald subjects had an SNR gain [Fig. 10(a)] because the brush optodes adapted better to the head curvature, and evaluation of Eq. (4), provided the insight that these gains originated from the matched boundary condition attained by the brush fibers that maintained good optical contact with the scalp. The improved optical contact enhanced the sensitivity to detect light coming from the cortical regions. Taken together, the above findings suggest that brush optodes could create useful images at hair densities where the flat optodes could not (Fig. 9) because even if

only 10% of the fibers in a brush optode could attain good optical contact with the scalp, these fibers could still glean enough signal to help form fNIRS images.

#### 4. Conclusions

A novel brush fiber attachment to the flat-faced detector optodes of a commercially available fNIRS system was developed to improve optical contact with the scalp. The performance of this optode during fNIRS measurements was tested on 17 subjects with varying hair colors and hair densities performing a finger tapping protocol with and without the brush optode attachments. The most salient finding of this work was that, in comparison to the flat-faced optodes, the brush optode attachments improved the SNR by up to a factor of ten [Figs. 8(a), 8(c), and 10(a)] making it possible for subjects with dark hair and high hair densities to be consistently measured successfully with fNIRS, which was not possible before. The increase in activation SNR by the brush optodes also led to a significant increase in dAoA ( $p < 0.05$ ) for both  $\Delta\text{HbO}$  and  $\Delta\text{Hb}$  data [Figs. 4 and 10(c)].

The source-detector arrangement was dense making it difficult to part hair, thus increasing the setup time when using the standard flat optodes (35–45 min.). This setup time was reduced by at least a factor of three (10–15 min.) when using the brush optodes due to their ability to readily thread through hair. In addition to the significant gains in setup time the improved optical contact with the scalp that the brush fibers enabled resulted in increasing the fNIRS study success rate to 100% (13/13) for the short haired subjects and to 3/4 from 1/4 for the long haired subjects. Also, the individual fibers of the brush-fiber optodes proved sturdy enough to undergo the pressure applied to achieve good optical contact for 34 sets of measurements and are still being used in current studies.

The improvement in fNIRS measurements was validated by MC simulations of the light intensity attenuation for subjects with different hair densities and hair colors. The comparison against the simulations showed very good agreement with the experimental data. Furthermore, an analytical model was derived from first principles to estimate the light power attenuation by the scalp and hair. Despite several simplifying assumptions, excellent agreement was attained between the analytical formula predictions and corresponding fNIRS measurements and MC simulations (Fig. 11). The derived analytical formula can therefore be a very useful tool, enabling researchers to estimate readily the power attenuation loss factor due to scalp and hair for a given subject and optode type.

It is noteworthy that the single long haired subject that could not be measured with the brush optodes could have possibly been measured too if the brushes were longer. For future studies, it is therefore advisable that a longer brush fiber set is also constructed to make it possible to thread through the thicker hair layers found in long hair subjects. Also, the SNR of human subject measurements could be further improved if the ~2.5 dB loss due to imperfect optical contact between the brush-fiber attachments and the commercial fNIRS system's fiber bundles [23] could be reduced by an improved optical coupling design. Despite current limitations the brush optodes present a technological leap towards improved NIR light collection.

Importantly, the brush fiber optode attachments can be molded to fit the diameter of any flat-faced fiber bundle in current commercial fNIRS systems and can thus be very useful for enhancing the success rates and reproducibility of fNIRS studies.

#### Acknowledgments

Support for this work was provided by the National Institute of Biomedical Imaging and Bioengineering (NIBIB), Grant No. 1R01EB013313-01, and by a University of Texas at Arlington/University of Texas at Dallas/Texas Instruments/Texas Health Resources Medical Technology Research Program Grant.